Effect of the Dispersion Medium on NMR Relaxation Properties of Superparamagnetic Iron Oxide Nanoparticles between 0.24 mT and 14.1 T

Lyns Verel Che Dji, Roua Kaddah, Thomas Girardet, Solenne Fleutot, Sabine Bouguet-Bonnet

Effect of the Dispersion Milieu on NMR Relaxation Properties of Superparamagnetic Iron Oxide Nanoparticles Between 0.24 mT and 14.1 T

Lyns Verel Che Dji[1,2], Roua Kaddah[2], Thomas Girardet[2], Solenne Fleutot[2], Sabine Bouguet-Bonnet[1*]*

[1]CRM[2] (Cristallographie, Résonance Magnétique et Modélisations), Université de Lorraine, CNRS, F-54500, Vandœuvre-lès-Nancy, France

[2]IJL (Institut Jean Lamour), Université de Lorraine, CNRS, F-5400, Nancy, France

KEYWORDS: Superparamagnetism, iron oxide nanoparticles, nuclear magnetic resonance dispersion profile, contrast agents.

ABSTRACT. Due to weak exchange interactions, magnetite particles at a critical diameter of about 20 nm are considered monodomain. At this size, they exhibit a phenomenological magnetic property called superparamagnetism, making them useful as Magnetic Resonance Imaging Contrast Agents, or MRI CAs. However, questions persist regarding the impact of using different physiological solvents and varying the environment in which these particles are dispersed on their performance, determined by their relaxivity. A colloidal suspension of superparamagnetic iron

oxide nanoparticles (SPIONs) electrostatically stabilized by citrate ligand was synthesized using a fast, reliable, and reproducible developed microwave approach, ensuring high stability over time at pH 7. We studied the effects of three physiological media on these MRI CAs. Ultra-pure water was used for the synthesis, while phosphate-buffered saline and physiological liquid were used to disperse the nanoparticles, as these media contain essential electrolytes for the functioning of the human body. The SPIONs underwent systematic characterizations to determine their physicochemical and magnetic properties. This study reports the longitudinal relaxivities of SPIONs at medically relevant magnetic field strengths. Field dependence of their relaxivity (efficacy) was evaluated using an Nuclear Magnetic Resonance Dispersion (NMRD) profile measured over a wide range of proton resonance frequencies between 5 kHz and 600 MHz. The Roch et al. model[30] was used to analyze the NMRD profile and evaluate the impact of SPIONs on water proton relaxation in the different redispersion media. It was observed in this study that the dynamics of water protons are not influenced by the redispersion media of these citrate-coated SPIONs. However, the presence of salt ions notably reduces their relaxivities by lowering the saturation magnetization of SPIONs.

INTRODUCTION: Materials at the nanoscale have a wide range of applications. They can be used in spintronics as nanomagnets to store informations[1], in the textile industry as nanofibers for producing smart textiles[2], and in civil engineering as insulators to reduce energy consumption[3]. The use of magnetic nanoparticles (MNPs) is also of great importance in biomedicine. They can be utilized for drug delivery by using the interaction between the nanoparticles NPs spin and an external magnetic field to direct drugs towards tumors[4,5]. MNPs can also induce a localized temperature increase through Néel or Brownian relaxation[6] processes, causing cell death, a therapeutic tool known as magnetic hyperthermia[7–10]. Additionally, their magnetic properties can be employed in diagnosis to enhance contrasts in magnetic resonance imaging (MRI), MNPs are then referred to as contrast agents (CAs)[8,11–15]. Combining these properties, MNPs can be used as nanotheranostic particles for in vivo applications, despite challenges[16].

MRI CAs are used to shorten water proton relaxation times. MNP CAs fall into two categories: the first one includes superparamagnetic iron oxide (SPIOs) which contain more than one crystal per particle. They are classified as negative MRI CAs because they shorten transverse magnetization time decay resulting in an enhanced T_2 effect. One example is Ferumoxide, commercially known as Feridex® or Endorem®, which is dextran-coated iron oxide nanoparticles IONPs clinically approved by the US Food and Drug Administration FDA in 1996 for liver and spleen imaging[12,17,18]. In 2009, it was however taken off the market due to synthesis control issues, limited applications, and other commercial reasons. The second category includes ultra-small superparamagnetic iron oxide (USPIO) or monocrystalline iron oxide nanoparticles (MIONs), which contain only one crystal per particle. They can be classified as both positive and negative MRI CAs because they also affect longitudinal magnetization time recovery leading to enhanced T_1 effects. Ferumoxtran, known commercially as Sinerem, Combidex, or Clariscan, is an example

of this category and is used for lymph node imaging [12,17,18]. Although these products were approved for use in clinics by some European countries, they never received clinical approval from the US FDA. Another example of USPIO is ferumoxytol commercially known as Feraheme®, a carboxymethyl dextran-coated IONPs that is not clinically approved as an MRI CA but rather as a treatment against iron deficiency anemia in patients with kidney failures. Nonetheless, recent research has demonstrated its use as a positive MRI contrast agent at very low field (64mT) MRI scanners[19].

The USPIO discussed in this work are citrate-coated. This coating enhances their colloidal stability and allows for control over their size distribution. Additionally, the citrate coating provides free negatively charged carboxylate groups on the particle surface, enabling the attachment of other compounds such as antibodies and drugs. These particles are also non-toxic at low concentrations[20] and their synthesis protocol ensures high reproducibility. This makes these USPIO suitable not only for use as MRI contrast agents but also for other applications. In our previous work[21], both the synthesis and redispersion milieu were varied but no detailed effect on water proton relaxation was investigated. This research aims to assess how three different milieus (ultra-pure water, physiological liquid, and phosphate-buffered saline solution), in which USPIO utilized as MRI CAs are dispersed, influence water proton relaxation. Several synthetic methods have been developed over time, including thermal decomposition[22], co-precipitation[23], hydrothermal[24] and solvothermal synthesis, and microwave synthesis[25]. Among these, microwave synthesis offers sample monodispersity, high yields, and short reaction times (seconds vs. hours) as demonstrated in a previous study[26]. The ease and speed of microwave synthesis, combined with the monodispersity of the samples, enable greater control over the physicochemical characteristics and magnetic properties, making it the preferred choice in this work.

To our knowledge, few studies have investigated the effect of IONPs dispersion environment on their relaxation properties[21,27]. Since IONPs are primarily used in the human body, where various molecules can impact water proton relaxation, it is crucial to carefully assess these effects. The influence of the dispersion milieu on water proton relaxations is often correlated with nanoparticle surface coating[27–29]. However, these two parameters are distinct and may have different effects when both are varied simultaneously. In this study, we aim to investigate how different milieus (isotonic with human blood) in which IONPs are dispersed affect water proton relaxations while maintaining citric acid as the capping agent.

Theoretical background

The efficacy of MRI IONPs-based CAs in terms of relaxation can be measured using equation (1).

$$\frac{1}{T_i} = R_i = r_i[C] + \frac{1}{T_{i0}} \quad i = 1,2 \tag{1}$$

Where R_i water proton relaxation rate is measured in s^{-1}, the slope r_i of the straight-line equation, known as relaxivity, is the increase in relaxation rate of water protons induced by 1 mmol L^{-1} IONPs, measured in s^{-1} mM^{-1}, $[C]$ concentration of IONPs in mmol L^{-1} and $\frac{1}{T_{i0}}$ is the relaxation rate of water protons in the solvent without IONPs.

Nuclear magnetic resonance (NMR) longitudinal relaxation times, T_1, were measured as a function of the magnetic field strengths. This measurement provides a plot called Nuclear Magnetic Resonance Dispersion NMRD profile, which is considered a fundamental tool for studying the relaxation properties of MRI contrast agents. In this study, these profiles were analyzed using the Roch et al.[30] theoretical model. Obtaining and analyzing NMRD profiles serve as a method for both characterizing IONPs[31] and predicting their efficacy at any magnetic field

strength in MRI. Physicochemical and magnetic properties such as Néel relaxation time, crystal anisotropy energy, the average radius of nanoparticles, and saturation magnetization are obtained.

This article discusses a detailed comparison of the impact of three different dispersion media of IONPs on water proton relaxation. The comparison relies on systematic physicochemical characterization techniques such as electron transmission microscopy, magnetometry, dynamic light scattering, thermogravimetric analysis, and x-ray diffraction. NMRD profiles were obtained and carefully analyzed. The physicochemical and magnetic parameters obtained were then compared to those obtained through the previously mentioned techniques, and consistent outcomes were observed.

SPIONs-induced water proton relaxation theories: a brief review

Water protons in the vicinity of unpaired electrons experience significantly shortened NMR relaxation times. These electrons may come from paramagnetic compounds e.g. Gadolinium chelates or superparamagnetic particles like IONPs. The Solomon-Bloembergen-Morgan (SBM) theory[31] predicts relaxation induced by paramagnetic substances, with chemical exchange being the key relaxation process. Conversely, the Roch-Muller-Gillis (RMG) or Roch et al.[30] theory predicts relaxation induced by superparamagnetic entities, based on Ayant[32] and Freed's[33] spectral densities. There are three significant distinctions between the two types of CA: (i) Paramagnetic compounds mainly shorten T_1 relaxation time while superparamagnetic entities mainly shorten T_2 relaxation time, with the former called positive and the latter negative CAs. (ii) Superparamagnetic particles have high saturation magnetization values making relaxation more effective than in paramagnetic compounds; and (iii) an intrinsic property known as internal anisotropy energy provides magnetic moments in superparamagnetic particles a preferred alignment direction called easy axis (often uniaxial). This feature is responsible for the difference in NMRD profiles, that is

the evolution of relaxation rate as a function of the magnetic field, between paramagnetic and superparamagnetic compounds.

In the case of water proton relaxation induced by SPIONs, also known as outer sphere relaxation mechanism[32,33] which is the basis of this study, relaxation arises from the magnetic dipolar interaction between electronic magnetic moments and nuclear magnetic moments. This occurs via two main processes; (i) when saturation of electronic magnetic moments, a local demagnetizing field (magnetic dipole approximation[34]) is generated. Nearby water molecules diffusing across this demagnetizing sphere experience rapid relaxation due to the fluctuation of their magnetic moments, defined by their precession with different proton Larmor frequencies. This process is time-modulated by the translational diffusion correlation time τ_D and referred to as Curie relaxation dominant at high fields ($B_0 > 0.02$ T)[30]. Another relaxation process undergone by water protons (ii) comes from the flip-flop motion of the electronic magnetization along its easy axis at low field, governed by Néel relaxation time τ_N[6]. Hence, the relaxation of water protons in the vicinity of SPIONs is based on the competition between these two relaxation mechanisms, Néel relaxation dominates at low-field, and Curie relaxation dominates at high field. Relaxation theories developed over time rely on the aforementioned mechanisms. Few groups were involved in its development.

In 1992, Roch and Muller proposed the first theory[35] for water proton relaxation induced by SPIONs. In this groundbreaking study, the authors focused on the relaxation behavior of large particles (SPIO) which mainly experience Brownian relaxation[6], so that their magnetic moments are found closer to their easy axes, resulting in little or no precession in the static magnetic field before alignment. In contrast, smaller particles (USPIO) have a larger angle between their magnetic moments and easy axes, resulting in some precession in the static magnetic field before

alignment. So, their theory[30] could not accurately model the low field part of the NMRD profile of USPIO because the internal anisotropy energy, responsible for this behavior, was not explicitly quantified. Another group, Koenig and Kellar, formulated a theory in 1995[36,37] that did not account for the internal anisotropy energy and could not be verified due to insufficient experimental data. In 1998, Bulte et al[38–40] developed their theory based on Koenig and Kellar's work. They incorporated a paramagnetic contribution to the relaxation process based on magnetometry measurements, considering the incomplete saturation of the electronic magnetic moments. This property is often observed in superparamagnetic particles due to their sensitivity to random thermal fluctuations. While experimental data supported their theory, it is not widely used to analyze NMRD profiles due to certain approximations and hypotheses used[41]. These include a significant number of fitting parameters, an assumption that an anti-ferromagnetic inclusion is responsible for the high field behavior of transverse relaxation rate, and paramagnetic contribution that may arise from the nanoparticle's surface.

In 1999, Roch, Muller, and Gillis came up with a quite complete quantum mechanical formulation[30] of water proton relaxation induced by SPIONs. In contrast to their previous work, the relaxation equations included the internal anisotropy energy as an explicit parameter. However, this was a topic of discussion in their study[42]. They then developed a heuristic model that linearly combines an infinite and zero internal anisotropy energy for efficient implementation and calculation time. The Roch et al.[30] model is now widely recognized as the preferred choice for analyzing NMRD profiles of SPIONs in particular.[27,29,43–45] It forms the basis of a spin-lattice relaxation model[46] developed to expand the range of proton dynamics, by using different solvents at varying temperatures. It is worth mentioning that earlier efforts to analyze the NMRD profile of nickel nanoparticles using the Roch et al.[30] model have been unsuccessful[47], as the theory

necessitated an extra calibration in the form of a weighing factor for Langevin's function. This is because nickel has a higher magnetic susceptibility than iron. Although the Roch et al.[30] model has been successful in many aspects, a limitation has been discovered over the years. An effort to examine the transverse NMRD profile of SPIONs was unsuccessful[41,43] as there was a discrepancy between experimental measurements and theoretical predictions at high fields. A new approach to the theory of magnetic nanoparticles-induced water proton relaxations was developed in 2016 by Rollet et al.[48]. This approach focuses on cobalt ferrite nanoparticles and is also based on Ayant[32] and Freed's[33] spectral densities.

In summary, research on the impact of SPIONs on water proton relaxations is still ongoing, and multiple theories exist without a clear consensus. Bulte et al's[38-40] model differs from others due to its 'three iron-phase' model, which is based on paramagnetic, small, and large superparamagnetic inclusions contributing to both longitudinal and transverse relaxation of water protons. It's worth noting that their theory does not account for anisotropy energy. Roch et al.'s[30] model is widely used and was developed for the analysis of SPIONs' NMRD profiles. This makes it suitable for our study, especially for our low anisotropic particles, as previous attempts with different particles e.g., nickel nanoparticles were unsuccessful[47]. Rollet et al's[48] model can be viewed as a generalized one, as they explored the NMRD profile of highly anisotropic particles, uncovering dynamics not addressed by other models, referred to as 'Rigid dipole'.

Experimental section

Materials and Synthesis

Functionalized IONPs were synthesized by the microwave method. To form a solution of iron precursor, Alfa Aesar's ferrous chloride tetrahydrate ($FeCl_2 . 4H_2O$ CAS N° 13478-10-9) and ferric chloride hexahydrate ($FeCl_3 . 6H_2O$ CAS N° 10025-77-1) were dissolved in 15 mL of ultra-pure

water (resistivity 18.2 mΩ cm at 25 °C) in a ratio of 1:2. 0.6 g citric acid monohydrate ($C_6H_8O_7$. H_2O CAS N° 5949-29-1) and 5 mL alkaline solution NH_4OH (CAS N° 1336-21-6) from Sigma Aldrich were added to the solution and thoroughly stirred until completely dissolved, resulting in a dark-colored solution. A magnetic stir bar was added before inserting the solution into the microwave oven. The mixture was then heated at 96°C for 40 minutes with constant magnetic stirring at 1080 rpm and a maximum power of 850 W.

After obtaining a solution of nanoparticles, they underwent two washing and purification cycles before resuspending in corresponding solvents. The first washing and purification step was performed using 20 mL of absolute ethanol, followed by centrifugation at 10,000 rpm for 10 minutes. The second step was performed using 10 mL of the corresponding solvent and 20 mL of absolute ethanol and centrifuged at 10,000 rpm for 10 minutes. One part of the solution was dried at 80°C for 24 hours, while the other part was kept in solution for further characterization. The mother solution had an initial concentration of approximately 20 g L^{-1}. Seven different dilutions are made, ranging from 12.5 µg mL^{-1} to 800 µg mL^{-1}, for relaxivity measurements.

To ensure unbiased comparisons between solvents that may arise from different syntheses, only one synthesis was carried out and then divided into three portions, one for each corresponding solvent. Following the synthesis in ultra-pure water, nanoparticles were named based on the resuspension medium: NPs_{ww} in ultra-pure water, NPs_{wphi} in physiological liquid (PHI, commercially available contains 9 g L^{-1} NaCl), and NPs_{wpbs} in phosphate-buffered saline solution (PBS, commercially available contains 8 g L^{-1} NaCl, 0.2 g L^{-1} KCl, 1.4 g L^{-1} Na_2HPO_4 and 0.2 g L^{-1} KH_2PO_4).

Experimental technique

Magnetic measurements of powder samples were conducted using a Physical Property Measurement System (PPMS) equipped with a Vibrating Sample Magnetometry (VSM) Quantum Design head operating at 14 T. Magnetization dependence of the applied magnetic field strength was recorded between -50,000 Oe and +50,000 Oe at 300 K and 5 K. Zero-field-cooled (ZFC) and field-cooled (FC) curves were measured in the temperature range of 5 K to 300 K with an applied magnetic field of 75 Oe.

X-ray diffraction of powder samples was performed between 10 and 90 (2theta) degrees on a D8 ADVANCE diffractometer from BRUKER equipped LYNXEYE detector for fluorescence filtering and a copper X-ray radiation source (Kα = 0.15406 nm). Information on the iron oxide phase was determined.

Shape and core size distribution of nanoparticles were obtained by Transmission electronic microscopy (TEM). Two drops of nanoparticle solution at a 0.3 mg mL^{-1} concentration were set on copper-grid carbon foils and allowed to dry. TEM was performed using a CM200-FEI, which operates at 200 kV and has a lanthanum hexaboride (LaB_6) electron source of wavelength 0.0025 nm.

The hydrodynamic size distribution of nanoparticles at 0.3 mg mL^{-1} concentration (independent of our concentration range) was measured by dynamic light scattering on a ZETASIZER Nano ZS device from Malvern Panalytical. To ensure accurate results, three measurements of 10 runs each were performed and the average was taken to determine the hydrodynamic diameter and its standard deviation.

Magnetic and NMR relaxation data were corrected based on the inorganic core's (iron oxide) percentage contribution only, using thermogravimetric analysis. The analysis was performed using

a SETSYS EV 1750 TGA microbalance from Setaram. The heating temperature ranged from 20-600°C at 10°C min^{-1} under air (20 mL min^{-1}).

NMR relaxation times T_1 and T_2 were measured at 37°C across a wide range of magnetic field strengths using different instruments. Low field T_1 relaxation times were measured at magnetic field strengths corresponding to 5 KHz-10 MHz (proton-Larmor frequency) using the Fast-Field Cycling (FFC) technique on a SMARTracer relaxometer from STELAR. A pre-polarization (PP) sequence at 8 MHz was applied between 5 KHz and 4 MHz to enhance sensitivity. This was followed by a non-polarization (NP) sequence between 4 MHz and 10 MHz. Signal acquisition was performed at 7.2 MHz. A switching time of 3 ms was set for rapid change of the magnetic field value, and the magnetization curve was fitted over 16 points (tau delay). Additional low field T_1 and T_2 relaxation times were measured using the inversion-recovery and CPMG (Carr-Purcell-Meiboom-Gill) sequences respectively on Bruker Minispec mq20, mq40, and mq60 (20 MHz, 40 MHz, and 60 MHz respectively). The T_1 relaxation time at high fields was measured using a saturation-recovery sequence on spectrometers operating at different frequencies. These included a 200 MHz spectrometer (4.7 T Oxford magnet and NMRCube console manufactured by RS2D), as well as Bruker Avance III spectrometers operating at 300 MHz, 400 MHz, and 600 MHz. To obtain longitudinal magnetization recovery curves, measurements were taken using 16 different evolution times ranging from 1 ms to $5T_1$. Meanwhile, the transverse magnetization decay curves were obtained by optimizing the CPMG sequence. This was done by adjusting the interpulse delay tau (which is the delay between the first 90° and 180° pulse) and the number of echoes. We set this delay to fall between 0.06 and 1.5 ms, and the number of echoes to fall between 125 and 1024 to cover the seven concentrations used in this study.

Result and discussion

Morphological and structural analysis

The micrographs (under bright field) of the three samples are presented in **Figure 1**, which clearly shows monodispersed, little or no aggregation state, and well-defined spherical shape nanoparticles.

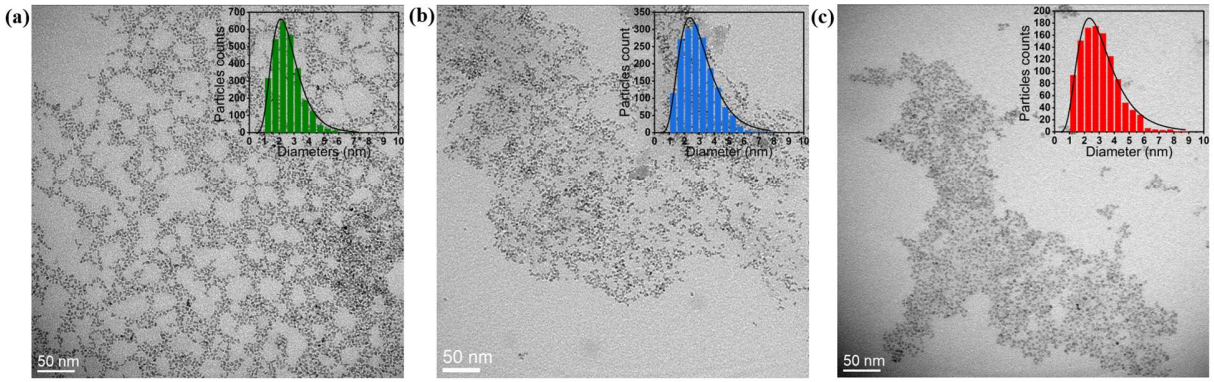

Figure 1. TEM micrographs of samples (a) NPs_{ww} (b) NPs_{wphi} and (c) NPs_{wpbs}, size distribution histogram fitted with a log-normal function.

Over a thousand nanoparticles were counted using ImageJ software based on automatic contrast-related counting. The resulting histogram was fitted with a log-normal function. The average diameters and standard deviations are reported in **Table 1**. Globally, all three samples exhibited the same average inorganic core diameter: 2.6 $\pm$ 1.1 nm, 3.1 $\pm$ 1.3 nm, and 3.2 $\pm$ 1.5 nm for NPs_{ww}, NPs_{wphi}, and NPs_{wpbs} respectively. The slight difference between NPs_{ww} on one side and NPs_{wphi} and NPs_{wpbs} on the other may be due to accumulated errors from the instrument and ImageJ software. However, considering the standard deviations, core diameters remain in the same order of magnitude.

Table 1

TEM size, hydrodynamic diameter (DLS), saturation magnetization (VSM, 300K, and 5K), and inorganic core (iron oxide) contribution by TGA for the three samples as a function of the dispersant medium.

Sample	Dispersant	Diameter (nm)		M_{sat} (emu g^{-1})		Iron oxide (%)
		<TEM>	<DLS>	300 K	5 K	
NPs_{ww}	Water	2.6 ± 1.1	10 ± 2	50	72	55.3
NPs_{wphi}	PHI	3.1 ± 1.3	8 ± 2	37	50	65.8
NPs_{wpbs}	PBS	3.2 ± 1.5	6 ± 1	35	50	66.2

The XRD patterns for all samples are shown in **Figure 2,** we observed similar peaks at the same angles. Phase determination was performed for all samples using magnetite (PDF 00-065-0731) as a reference, which showed a lattice parameter of 0.8375 nm and crystallization in the space group F_{d3m}. The lattice parameter found for our nanocrystals lies between that of reference magnetite (0.8385 nm) and maghemite (0.8354 nm). This indicates that our nanocrystals possess a deviation from stoichiometry, possibly due to an insufficient amount of oxygen in the inverse spinel crystal lattice structure. The XRD patterns do not clearly distinguish between magnetite and maghemite iron phases. In a previous work[49], Mössbauer and Raman spectroscopies were used to determine the percentage of magnetite in these particles obtained with an optimized synthesis protocol, the nanoparticles (inorganic core) were characterized as magnetite with a slight oxidation state (sub-stochiometric magnetite particles).

In samples NPs_{wphi}, and NPs_{wpbs}, new peaks were identified compared to NPs_{ww}. These peaks were identified with sodium chloride phase (PDF 04-016-2944), indicating the formation of NaCl matrix in both samples. This is because physiological liquid and phosphate-buffered saline are solvents

with high salt content. Since both TEM and XRD provide information about the inorganic core, an investigation of the organic layer was carried out by DLS.

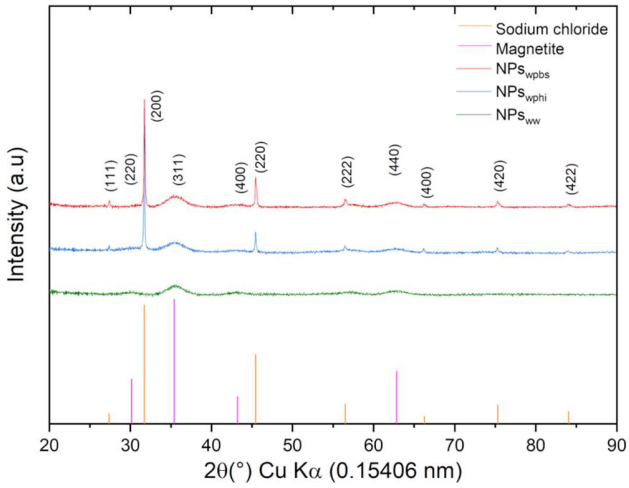

Figure 2. XRD patterns of NPs_{ww} (green), NPs_{wphi} (blue), and NPs_{wpbs} (red) identified with magnetite reference PDF 00-065-0731(purple) and sodium chloride PDF 04-016-2944 (orange).

Investigation of colloidal stability showed NPs_{ww} had a negative zeta potential of -34 mV at 0.2 mg mL^{-1} in ultra-pure water. Because of the high salt content in NPs_{wphi} and NPs_{wpbs} zeta potential measurements were unstable. DLS experiments showed a significant increase in the diameters of various samples, as presented in **Table 1** and **Figure 3**. This increase corresponds to an additional layer on the surface. Indeed, DLS allows for the measurement of the hydrodynamic diameter encompassing the inorganic core diameter, and the organic layer, as well as a solvation layer. The substantial increase in diameters corresponds to the size of the organic and solvation spheres. Surface functionalization was confirmed in our previous work[26] on optimizing this synthesis protocol. This was achieved by varying synthesis factors such as ramp time, stage time, temperature, microwave power, and stirring duration. Fourier-Transform Infrared Spectroscopy

and Thermogravimetric Analysis confirmed an organic and solvation sphere at the surface of the nanoparticles.

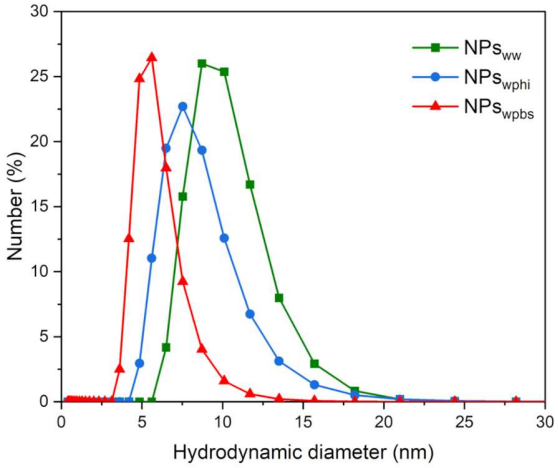

Figure 3. DLS number size distribution of NPs_{ww} (green), NPs_{wphi} (blue), and NPs_{wpbs} (red).

Magnetic characterization

Figure 4a displays magnetic moment dependence with the applied magnetic field M(H) at room temperature, conducted on powder. At this temperature, no hysteresis was observed, which indicates that the nanoparticle's magnetic moments are in a superparamagnetic state. This occurs in certain materials such as ferromagnets, ferrimagnets (magnetic state of magnetite at the macroscopic scale), and antiferromagnets when their sizes are reduced to the nanometric scale, such that they are considered monodomain (single-particle behavior). In the absence of an external magnetic field, there is no net macroscopic magnetization. This occurs because the random alignment of magnetic moments, caused by thermal fluctuations, overcomes the magnetic anisotropy energy barrier. As a result, magnetic moments jump from one easy direction to another, causing the average magnetization to be zero as long as the measurement time is greater than the average time between flips. These particles are often characterized by a low coercive field and little or no remanant magnetization. A uniaxial symmetry is assumed in this context. Saturation

magnetization values were obtained by fitting Langevin's function at 300 K (see **Figure S1)**. The values obtained were 50 emu g^{-1} for NPs_{ww}, 37 emu g^{-1} for NPs_{wphi}, and 35 emu g^{-1} for NPs_{wpbs}. These values were corrected based on TGA **(Table 1)** to take only into account the inorganic core for the weight of the material. It is worth noting that there is a noticeable decrease in saturation magnetization in NPs_{wphi} and NPs_{wpbs}. This decrease may be attributed to the diamagnetic nature of the salt content found in these samples, as evidenced by XRD.

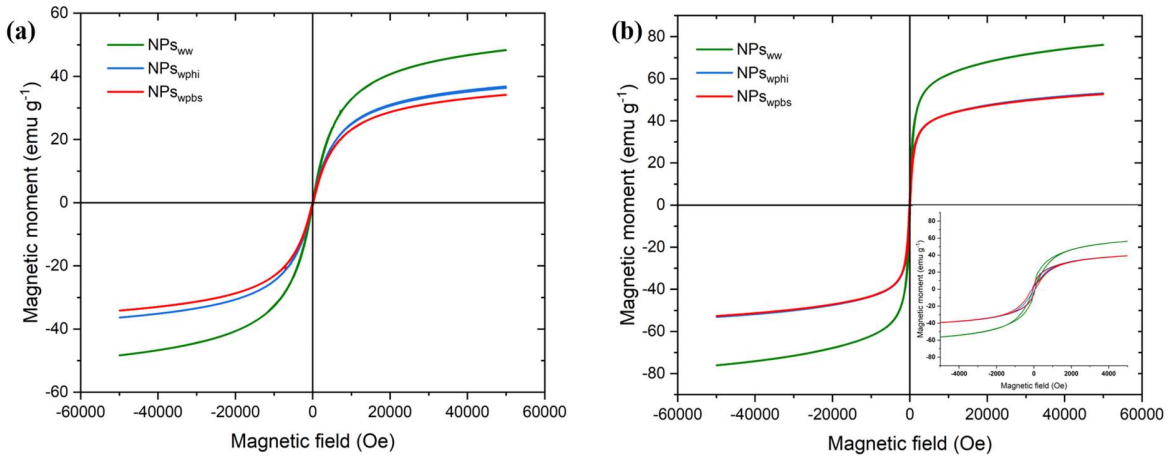

Figure 4. Magnetic measurements indicate saturation magnetization M(H) curves at (a) 300 K and (b) 5K. Inset: zoom to show the low-field region at 5K.

Temperature dependence of the superparamagnetic state was evaluated by Zero Field Cooling (ZFC) and Field Cooling (FC) curves, as displayed in **Figure S1a**. The maximum of the ZFC curves corresponds to a blocking temperature distribution of 17 K for all three samples. Below this temperature, M(H) curves measured at 5 K (**Figure 4b)** demonstrated a relative increase in saturation magnetization compared to the measurements at 300 K. Additionally, a zoomed-in inset at low fields displayed loop-like behavior. These observations strongly indicate a transition of the magnetic moments from a superparamagnetic state at room temperature to a blocked state at 5 K.

Longitudinal r_1 NMRD profile

Figure 5a displays the longitudinal r_1 NMRD profiles obtained for all three samples at 37°C. Experimental r_1 data were calculated from the linear regression of the relaxation rate R_1 against different concentrations (refer to **Figure S2**) and corrected by TGA to have a relaxivity value related to the mass of iron oxide only.

The Roch et al.[30] heuristic model given below was used to fit the experimental data.

$$r_1 = \frac{32\pi}{135{,}0000}\left(\frac{\mu_0}{4\pi}\right)^2 \gamma_I^2 N_A C \times \left(\frac{\mu_{spm}^2}{r_{diff}.D}\right) \times [7\frac{L(\alpha)}{\alpha} P J_F(\omega_S, \tau_D, \tau_N) + 7(1-\mathrm{P})\frac{L(\alpha)}{\alpha} J_F(\omega_I, \tau_D, \tau_N) + 3\left(1 - L^2(\alpha) - 2\frac{L(\alpha)}{\alpha}\right) J_F(\omega_I, \tau_D, \tau_N) + 3L^2(\alpha) J_A(\omega_I, \tau_D)] \quad (2)$$

With,

$$J_F(\omega, \tau_D, \tau_N) = Re\left(\frac{1+\frac{1}{4}\Omega^{1/2}}{1+\Omega^{1/2}+\frac{4}{9}\Omega+\frac{1}{9}\Omega^{3/2}}\right), \qquad \Omega = i\omega\tau_D + \frac{\tau_D}{\tau_N}$$

$$J_A(\omega_I, \tau_D) = \frac{1+\frac{5u}{8}+\frac{u^2}{8}}{1+u+\frac{u^2}{2}+\frac{u^3}{6}+\frac{4u^4}{81}+\frac{u^5}{81}+\frac{u^6}{648}}, \qquad u = \sqrt{2\omega_I\tau_D}$$

Where μ_0 is the permeability of free space, γ_I is the proton gyromagnetic ratio intrinsic to the considered nucleus, N_A is the Avogadro's number, C is the concentration of Fe_3O_4 equals 1 mmol.L^{-1}, μ_{spm} is the magnetic moment of the nanoparticles, r_{diff} is the minimum distance of approach of water molecules relative to the electronic magnetization, D is the proton diffusion coefficient, $L(\alpha)$ is the Langevin's function with $\alpha = \mu_{spm}B_0/(K_BT)$, P is a coefficient from the linear combination of anisotropy energies, for $E_A \to \infty$, $P = 0$ and for $E_A \to 0$, $P = 1$, ω_S and ω_I are the electronic and proton Larmor frequencies respectively, J_A and J_F represent Ayant's[32] and Freed's[33] spectral densities respectively, τ_N is the Néel relaxation and τ_D is the translational diffusion correlation time given by r_{diff}^2/D.

A MATLAB[50] script was developed to perform the fitting process using the built-in 'fminsearch' function. The script used varying parameters r_{diff}, τ_N, μ_{spm}, D, and P. A Monte Carlo procedure was implemented to obtain the uncertainties on these fitting parameters and to verify the convergence of the fitting procedure through over 4096 iterations. Different initial conditions were tested and the results consistently confirmed the convergence of this fitting procedure. The results are summarized in **Table 2**. The saturation magnetization M_{sat} was calculated from μ_{spm} and the result was compared to the values obtained from VSM. The comparison showed consistent results, but it's important to note that the measurements were conducted in different states of matter, in which dipolar interactions differ. VSM measurement was carried out on powder (solid), where magnetic dynamics can mainly be explained by the Néel relaxation model[6] and temperature dependence of the dynamics by the Vogel-Fulcher-Tammann model[51–53]. In contrast, NMR was performed on a colloidal solution of nanoparticles. The slight discrepancy in values may be explained by the nature of dipolar interactions in these two states and also by the fact that Roch et al.'s model was developed for the case of non-interacting particles. NMR gave an average diameter ($2r_{diff}$) that remarkably falls in between the values obtained from DLS and MET (**Table 1**). According to Roch et al.'s[30] theory, r_{diff} reflects the diffusion of water molecules relative to the demagnetizing field created by the electronic magnetization. In the case of our citrate-coated nanoparticles, the value of r_{diff} may therefore be influenced by the permeability of this ligand.

Table 2

Data extracted (r_{diff}, τ_N, μ_{spm}, D, and P) from the analysis of the longitudinal r_1 NMRD profiles using Eq. (2) (error estimate based on 4096 Monte Carlo iterations) and the calculated saturation magnetization values ($M_{sat,NMR}$).

Samples	r_{diff} (10^{-9} m)	τ_N (10^{-10} s)	μ_{spm} (10^{-20} A m^2)	D (10^{-9} m^2 s^{-1})	P	$M_{sat,NMR}$ (emu g^{-1})
NPs_{ww}	2.2 ± 0.2	8.9 ± 0.5	4.8 ± 0.6	2.8 ± 0.6	0.3 ± 0.05	52
NPs_{wphi}	2.4 ± 0.2	7.7 ± 0.5	4.4 ± 0.6	2.8 ± 0.7	0.3 ± 0.05	48
NPs_{wpbs}	2.6 ± 0.2	8.5 ± 0.5	3.9 ± 0.4	2.4 ± 0.4	0.3 ± 0.05	43

In **Figure 5a**, it is observed that there is a shift of the NMRD profiles from NPs_{wpbs} to NPs_{ww} towards higher values of relaxivity across all proton Larmor frequencies. This shift is not due to the difference in composition (salts) of the redispersion media, as NMRD measurements performed on water protons of the three solvents alone (without NPs) gave the same longitudinal relaxation values over the entire ^{1}H frequency range (data not shown). Nor can this discrepancy be explained by a difference in pH between the three media[45]. Indeed, in the pH range measured here, i.e. 6.5-7.5, the corrections on the NMRD curves are negligible compared to the observed shifts.

Actually, upon normalizing the low-frequency experimental data (for each dispersion medium, raw data have been divided by the average r_1 between 0.005 and 0.12 MHz) to obtain a master curve, a perfect superposition of all NMRD curves was obtained (see **Figure 5b**). This is a clear indication that the dynamics (correlation times and diffusion rates) of water protons in the three samples are the same. Thus, the decrease in r_1 in NPs_{wphi} and NPs_{wpbs} may be correlated to the presence of the NaCl matrix (revealed by XRD), which leads to a decrease in saturation magnetization values. Indeed, as shown in simulations of **Figure S3**, as saturation magnetization decreases, so does water proton relaxation. This is because the strength of the demagnetizing field

created by the electronic magnetization, which is related to saturation magnetization value, also decreases. As a result, water protons diffusing across this field experience slower relaxation.

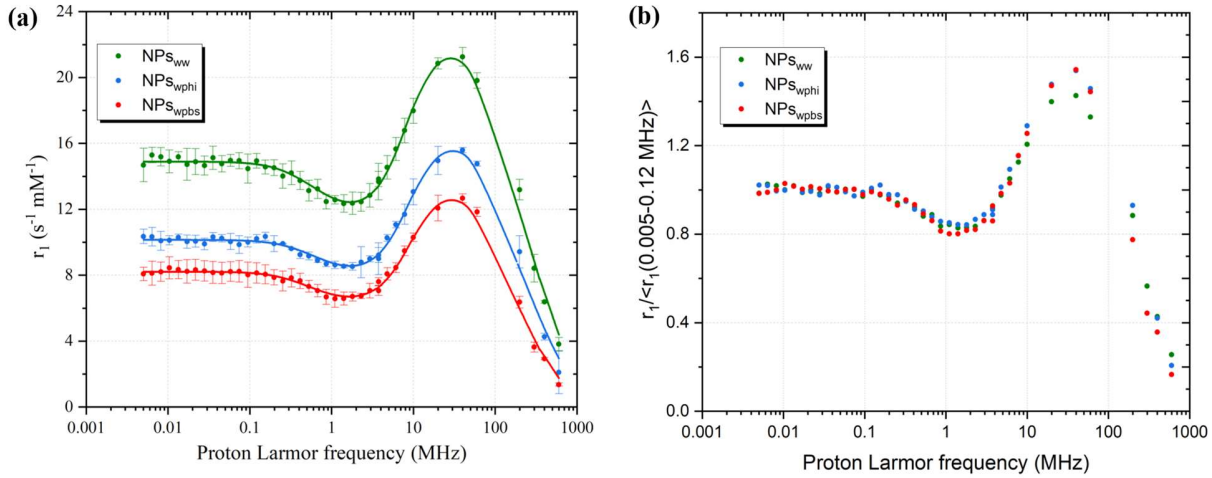

Figure 5. (a) Comparison of the analyzed longitudinal r_1 NMRD profiles of NPs_{ww} (green), NPs_{wphi} (blue), and NPs_{wpbs} (red) at 37°C in the frequency range 0.005-600 MHz and (b) calculated ratio $r_1/<r_1(0.005\text{-}0.12\ MHz)>$.

It is demonstrated here that, Roch et al.[30] theory accurately modeled the longitudinal r_1 NMRD profiles obtained on citrate-coated SPIONs in different redispersion media, leading to the extraction of important physicochemical parameters that could be compared to those obtained by other methods (TEM, XRD, DLS, magnetometry). Very consistent outcomes were observed, demonstrating the value of low-field relaxometry measurements for a complete characterization of SPIONs as MRI contrast agents.

The NMRD profiles we obtained showed that these citrate-coated USPIO are most efficient for a positive contrast at 40-60 MHz (0.9-1.4 T), which corresponds to the magnetic field strength typically used in medical MRI (1.5 T). Therefore, these particles are optimal for use as MRI CAs in this field range. We also measured transverse relaxation time T_2 in this range of magnetic fields

to investigate the efficacy of these particles as negative MRI CAs, as reported in **Table 3**. It can be seen that the SPIONs synthesized in this work can be used as both T_1 and T_2 contrast agents.

Table 3

Longitudinal and transverse relaxivities measured at 40 MHz (0.9 T) and 60 MHz (1.4 T) and 37°C.

Sample	r_1 (s^{-1} mM^{-1})		r_2 (s^{-1} mM^{-1})	
	40 MHz	60 MHz	40 MHz	60 MHz
NPs_{ww}	21.3 ± 0.6	19.8 ± 0.5	46.6 ± 1.4	52.5 ± 1.2
NPs_{wphi}	15.6 ± 0.2	14.8 ± 0.2	35.2 ± 0.5	40.7 ± 1.8
NPs_{wpbs}	12.7 ± 0.3	11.9 ± 0.3	30.1 ± 0.5	34.4 ± 0.5

Conclusion

This study provides a comprehensive analysis of the relaxation properties of superparamagnetic iron oxide nanoparticles (SPIONs) across a wide proton frequency range, corresponding to a magnetic field range of 0.24 mT to 14.1 T. The results clearly demonstrate that the SPIONs synthesized using the microwave approach, coated with citrate, and with an average inorganic core diameter of 3 nm, are excellent candidates for use as contrast agents in MRI. Three distinct physiological media were tested for the redispersion of the nanoparticles: ultrapure water, physiological liquid, and phosphate-buffered saline solution. The SPIONs underwent systematic characterizations to determine their physicochemical and magnetic properties, and their performance as contrast agents was evaluated by measuring their longitudinal relaxivity as a function of the magnetic field using a fast field cycling NMRD approach.

The NMRD profiles acquired in the three different physiological media were carefully analyzed, yielding the following findings: (i) consistent physicochemical parameters can be directly obtained from the NMRD profiles, with consistency verified through various characterization methods; (ii) the redispersion media do not affect the SPIONs' dynamics in solution; and (iii) the SPIONs synthesized in this study are suitable for use as contrast agents at magnetic fields typically employed in medical MRI. It was also observed that the SPIONs can function as both T_1 and T_2 contrast agents.

Furthermore, this study highlights that NMRD is an innovative methodological approach that allows for the rapid acquisition of the physicochemical and magnetic properties of SPIONs. It is also invaluable for characterizing the relaxation properties of the nanoparticles over a broad magnetic field range, facilitating the determination of the most suitable field for medical MRI applications.

ASSOCIATED CONTENT

Supporting Information.

Supporting information: ZFC/FC curves for all samples and fitted M(H) with Langevin's function; longitudinal relaxation rates R_1 and deduced longitudinal relaxivity r_1 NMRD profile of NPs_{ww}; simulated longitudinal relaxivity r_1 NMRD profiles for varying saturation magnetization values. (PDF)

AUTHOR INFORMATION

Corresponding Authors

*Sabine Bouguet-Bonnet – CRM^2 laboratory, University of Lorraine, CNRS, F-54500, Vandoeuvre-lès-Nancy, France. E-mail – sabine.bonnet@univ-lorraine.fr

*Solenne Fleutot – IJL laboratory, University of Lorraine, CNRS, F-54000, Nancy, France. E-mail - solenne.fleutot@univ-lorraine.fr

Author Contributions

This manuscript was written through the contributions of all authors. All authors have approved the final version of the manuscript.

Funding Sources

This research received no external funding.

Notes

The authors declare that they have no competing interests.

ACKNOWLEDGMENT

The authors acknowledge Younes Bouizi, for the NMR relaxation measurements at 200 MHz, Nadia Canilho for the pH and zeta potential measurements, and the CPM NMR facility of the University of Lorraine for the NMR relaxation measurements at high fields. In addition, regard goes to the microscopy and magnetism centers of the Institute Jean Lamour. Lyns Verel Che Dji acknowledges support from the French Ministry of Higher Education, Research and Innovation.

ABBREVIATIONS

NMRD, nuclear magnetic resonance dispersion; MRI CAs, magnetic resonance imaging contrast agents; SPIONs, superparamagnetic iron oxide nanoparticles; IONPs, iron oxide nanoparticles; MNPs, magnetic nanoparticles.

References

(1) Tahmasebi, T.; Piramanayagam, S. N. NANOSCIENCE AND NANOTECHNOLOGY FOR MEMORY AND DATA STORAGE. *COSMOS* **2011**, *07* (01), 25–30. https://doi.org/10.1142/S0219607711000705.

(2) Wan, L. Y. Nanofibers for Smart Textiles. In *Smart Textiles*; Yilmaz, N. D., Ed.; Wiley, **2018**; pp 39–90. https://doi.org/10.1002/9781119460367.ch2.

(3) Abdelrady, A.; Abdelhafez, M. H. H.; Ragab, A. Use of Insulation Based on Nanomaterials to Improve Energy Efficiency of Residential Buildings in a Hot Desert Climate. *Sustainability* **2021**, *13* (9), 5266. https://doi.org/10.3390/su13095266.

(4) Jaji, N.-D.; Lee, H. L.; Hussin, M. H.; Akil, H. M.; Zakaria, M. R.; Othman, M. B. H. Advanced Nickel Nanoparticles Technology: From Synthesis to Applications. *Nanotechnology Reviews* **2020**, *9* (1), 1456–1480. https://doi.org/10.1515/ntrev-2020-0109.

(5) Price, P. M.; Mahmoud, W. E.; Al-Ghamdi, A. A.; Bronstein, L. M. Magnetic Drug Delivery: Where the Field Is Going. *Front. Chem.* **2018**, *6*, 619. https://doi.org/10.3389/fchem.2018.00619.

(6) Ilg, P.; Kröger, M. Dynamics of Interacting Magnetic Nanoparticles: Effective Behavior from Competition between Brownian and Néel Relaxation. *Physical Chemistry Chemical Physics* **2020**, *22* (39), 22244–22259. https://doi.org/10.1039/D0CP04377J.

(7) Mornet, S.; Vasseur, S.; Grasset, F.; Duguet, E. Magnetic Nanoparticle Design for Medical Diagnosis and Therapy. *J. Mater. Chem.* **2004**, *14* (14), 2161. https://doi.org/10.1039/b402025a.

(8) Cortajarena, A. L.; Ortega, D.; Ocampo, S. M.; Gonzalez-García, A.; Couleaud, P.; Miranda, R.; Belda-Iniesta, C.; Ayuso-Sacido, A. Engineering Iron Oxide Nanoparticles for Clinical Settings. *Nanobiomedicine* **2014**, *1*, 2. https://doi.org/10.5772/58841.

(9) Dias, A. M. M.; Courteau, A.; Bellaye, P.-S.; Kohli, E.; Oudot, A.; Doulain, P.-E.; Petitot, C.; Walker, P.-M.; Decréau, R.; Collin, B. Superparamagnetic Iron Oxide Nanoparticles for Immunotherapy of Cancers through Macrophages and Magnetic Hyperthermia. *Pharmaceutics* **2022**, *14* (11), 2388. https://doi.org/10.3390/pharmaceutics14112388.

(10) Vangijzegem, T.; Lecomte, V.; Ternad, I.; Van Leuven, L.; Muller, R. N.; Stanicki, D.; Laurent, S. Superparamagnetic Iron Oxide Nanoparticles (SPION): From Fundamentals to State-of-the-Art Innovative Applications for Cancer Therapy. *Pharmaceutics* **2023**, *15* (1), 236. https://doi.org/10.3390/pharmaceutics15010236.

(11) Antonelli, A.; Magnani, M. SPIO Nanoparticles and Magnetic Erythrocytes as Contrast Agents for Biomedical and Diagnostic Applications. *Journal of Magnetism and Magnetic Materials* **2022**, *541*, 168520. https://doi.org/10.1016/j.jmmm.2021.168520.

(12) Thakor, A. S.; Jokerst, J. V.; Ghanouni, P.; Campbell, J. L.; Mittra, E.; Gambhir, S. S. Clinically Approved Nanoparticle Imaging Agents. *J Nucl Med* **2016**, *57* (12), 1833–1837. https://doi.org/10.2967/jnumed.116.181362.

(13) Zhang, S.; Merritt, M.; Woessner, D. E.; Lenkinski, R. E.; Sherry, A. D. PARACEST Agents: Modulating MRI Contrast via Water Proton Exchange. *Acc. Chem. Res.* **2003**, *36* (10), 783–790. https://doi.org/10.1021/ar020228m.

(14) Xu, X.; Dong, P.-L.; Chai, Y.-Y.; Yang, R.; Ma, Z.-H.; Lu, C.-C. Doping Engineering of Iron Oxide Nanoparticles towards High Performance and Biocompatible T_1-Weighted MRI Contrast Agents. *Rare Metals* **2024**, *43* (1), 298–308. https://doi.org/10.1007/s12598-023-02443-5.

(15) Wahsner, J.; Gale, E. M.; Rodríguez-Rodríguez, A.; Caravan, P. Chemistry of MRI Contrast Agents: Current Challenges and New Frontiers. *Chem Rev* **2019**, *119* (2), 957–1057. https://doi.org/10.1021/acs.chemrev.8b00363.
(16) Ojha, A. K.; Rajasekaran, R.; Pandey, A. K.; Dutta, A.; Seesala, V. S.; Das, S. K.; Chaudhury, K.; Dhara, S. Nanotheranostics: Nanoparticles Applications, Perspectives, and Challenges. In *BioSensing, Theranostics, and Medical Devices: From Laboratory to Point-of-Care Testing*; Borse, V., Chandra, P., Srivastava, R., Eds.; Springer: Singapore, **2022**; pp 345–376. https://doi.org/10.1007/978-981-16-2782-8_14.
(17) Wang, Y.-X. J.; Hussain, S. M.; Krestin, G. P. Superparamagnetic Iron Oxide Contrast Agents: Physicochemical Characteristics and Applications in MR Imaging. *Eur Radiol* **2001**, *11* (11), 2319–2331. https://doi.org/10.1007/s003300100908.
(18) Rahman, M. Magnetic Resonance Imaging and Iron-Oxide Nanoparticles in the Era of Personalized Medicine. *Nanotheranostics* **2023**, *7* (4), 424–449. https://doi.org/10.7150/ntno.86467.
(19) Oberdick, S. D.; Jordanova, K. V.; Lundstrom, J. T.; Parigi, G.; Poorman, M. E.; Zabow, G.; Keenan, K. E. Iron Oxide Nanoparticles as Positive T1 Contrast Agents for Low-Field Magnetic Resonance Imaging at 64 mT. *Sci Rep* **2023**, *13* (1), 11520. https://doi.org/10.1038/s41598-023-38222-6.
(20) Girardet, T.; Bianchi, E.; Henrionnet, C.; Pinzano, A.; Bouguet-Bonnet, S.; Boulogne, C.; Leclerc, S.; Cleymand, F.; Fleutot, S. SPIONs Magnetic Nanoparticles for MRI Applications: Microwave Synthesis and Physicochemical, Magnetic and Biological Characterizations. *Materials Today Communications* **2023**, *36*, 106819. https://doi.org/10.1016/j.mtcomm.2023.106819.
(21) Girardet, T.; Che Dji, L. V.; Bouguet-Bonnet, S.; Cleymand, F.; Fleutot, S. Rapid Microwave Synthesis of Magnetic Nanoparticles in Physiological Serum. *Pure and Applied Chemistry* **2022**, *94* (10), 1149–1159. https://doi.org/10.1515/pac-2022-0601.
(22) Park, J.; An, K.; Hwang, Y.; Park, J.-G.; Noh, H.-J.; Kim, J.-Y.; Park, J.-H.; Hwang, N.-M.; Hyeon, T. Ultra-Large-Scale Syntheses of Monodisperse Nanocrystals. *Nat Mater* **2004**, *3* (12), 891–895. https://doi.org/10.1038/nmat1251.
(23) Slimani, S.; Meneghini, C.; Abdolrahimi, M.; Talone, A.; Murillo, J. P. M.; Barucca, G.; Yaacoub, N.; Imperatori, P.; Illés, E.; Smari, M.; et al. Spinel Iron Oxide by the Co-Precipitation Method: Effect of the Reaction Atmosphere. *Applied Sciences* **2021**, *11* (12), 5433. https://doi.org/10.3390/app11125433.
(24) Kahil, H.; Faramawy, A.; El-Sayed, H.; Abdel-Sattar, A. Magnetic Properties and SAR for Gadolinium-Doped Iron Oxide Nanoparticles Prepared by Hydrothermal Method. *Crystals* **2021**, *11* (10), 1153. https://doi.org/10.3390/cryst11101153.
(25) Fernández-Barahona, I.; Muñoz-Hernando, M.; Herranz, F. Microwave-Driven Synthesis of Iron-Oxide Nanoparticles for Molecular Imaging. *Molecules* **2019**, *24* (7), 1224. https://doi.org/10.3390/molecules24071224.
(26) Girardet, T.; Kessler, M.; Migot, S.; Aranda, L.; Diliberto, S.; Suire, S.; Ferté, T.; Hupont, S.; Cleymand, F.; Fleutot, S. One Step Superparamagnetic Iron Oxide Nanoparticles by a Microwave Process: Optimization of Microwave Parameters with an Experimental Design. *Part & Part Syst Charact* **2024**, 2300226. https://doi.org/10.1002/ppsc.202300226.
(27) Basini, M.; Orlando, T.; Arosio, P.; Casula, M. F.; Espa, D.; Murgia, S.; Sangregorio, C.; Innocenti, C.; Lascialfari, A. Local Spin Dynamics of Iron Oxide Magnetic Nanoparticles

Dispersed in Different Solvents with Variable Size and Shape: A 1H NMR Study. *J Chem Phys* **2017**, *146* (3), 034703. https://doi.org/10.1063/1.4973979.
(28) Bordonali, L.; Kalaivani, T.; Sabareesh, K. P. V.; Innocenti, C.; Fantechi, E.; Sangregorio, C.; Casula, M. F.; Lartigue, L.; Larionova, J.; Guari, Y.; et al. NMR-D Study of the Local Spin Dynamics and Magnetic Anisotropy in Different Nearly Monodispersed Ferrite Nanoparticles. *J. Phys.: Condens. Matter* **2013**, *25* (6), 066008. https://doi.org/10.1088/0953-8984/25/6/066008.
(29) Arosio, P.; Orsini, F.; Brero, F.; Mariani, M.; Innocenti, C.; Sangregorio, C.; Lascialfari, A. The Effect of Size, Shape, Coating and Functionalization on Nuclear Relaxation Properties in Iron Oxide Core–Shell Nanoparticles: A Brief Review of the Situation. *Dalton Trans.* **2023**, *52* (12), 3551–3562. https://doi.org/10.1039/D2DT03387A.
(30) Roch, A.; Muller, R. N.; Gillis, P. Theory of Proton Relaxation Induced by Superparamagnetic Particles. *The Journal of Chemical Physics* **1999**, *110* (11), 5403–5411. https://doi.org/10.1063/1.478435.
(31) Conte, P. Chapter 10. Environmental Applications of Fast Field-Cycling NMR Relaxometry. In *New Developments in NMR*; Kimmich, R., Ed.; Royal Society of Chemistry: Cambridge, **2018**; pp 229–254. https://doi.org/10.1039/9781788012966-00229.
(32) Ayant, Y.; Belorizky, E.; Aluzon, J.; Gallice, J. Calcul des densités spectrales résultant d'un mouvement aléatoire de translation en relaxation par interaction dipolaire magnétique dans les liquides. *J. Phys. France* **1975**, *36* (10), 991–1004. https://doi.org/10.1051/jphys:019750036010099100.
(33) Freed, J. H. Dynamic Effects of Pair Correlation Functions on Spin Relaxation by Translational Diffusion in Liquids. II. Finite Jumps and Independent *T* 1 Processes. *The Journal of Chemical Physics* **1978**, *68* (9), 4034–4037. https://doi.org/10.1063/1.436302.
(34) Hardy, P. A.; Henkelman, R. M. Transverse Relaxation Rate Enhancement Caused by Magnetic Particulates. *Magn Reson Imaging* **1989**, *7* (3), 265–275. https://doi.org/10.1016/0730-725x(89)90549-3.
(35) A. Roch and R. N. Muller, Proceedings of the 11th Annual Meeting of the Society of Magnetic Resonance in Medicine, Works in Progress, **1992**, p. 1447.
(36) Koenig, S. H.; Kellar, K. E. Theory of 1/T1 and 1/T2 NMRD Profiles of Solutions of Magnetic Nanoparticles. *Magn. Reson. Med.* **1995**, *34* (2), 227–233. https://doi.org/10.1002/mrm.1910340214.
(37) Koenig, S. H.; Kellar, K. E. Theory of Proton Relaxation in Solutions of Magnetic Nanoparticles, Including the Superparamagnetic Size Range. *Academic Radiology* **1996**, *3*, S273–S276. https://doi.org/10.1016/S1076-6332(96)80555-1.
(38) Bulte, J. W. M.; Brooks, R. A.; Moskowitz, B. M.; Henry Bryant, L.; Frank, J. A. T1 and T2 Relaxometry of Monocrystalline Iron Oxide Nanoparticles (MION-46L): Theory and Experiment. *Academic Radiology* **1998**, *5*, S137–S140. https://doi.org/10.1016/S1076-6332(98)80084-6.
(39) Bulte, J. W. M.; Brooks, R. A.; M. Moskowitz, B.; Henry Bryant, L.; Frank, J. A. Relaxometry, Magnetometry, and EPR Evidence for Three Magnetic Phases in the MR Contrast Agent MION-46L. *Journal of Magnetism and Magnetic Materials* **1999**, *194* (1–3), 217–223. https://doi.org/10.1016/S0304-8853(98)00555-1.
(40) Bulte, J. W. M.; Brooks, R. A.; Moskowitz, B. M.; Bryant, L. H.; Frank, J. A. Relaxometry and Magnetometry of the MR Contrast Agent MION-46L. *Magn. Reson. Med.* **1999**, *42* (2),

379–384. https://doi.org/10.1002/(SICI)1522-2594(199908)42:2<379::AID-MRM20>3.0.CO;2-L.
(41) Vuong, Q. L.; Gillis, P.; Roch, A.; Gossuin, Y. Magnetic Resonance Relaxation Induced by Superparamagnetic Particles Used as Contrast Agents in Magnetic Resonance Imaging: A Theoretical Review. *WIREs Nanomedicine and Nanobiotechnology* **2017**, *9* (6), e1468. https://doi.org/10.1002/wnan.1468.
(42) Roch, A.; Muller, R. N.; Gillis, P. Water Relaxation by SPM Particles: Neglecting the Magnetic Anisotropy? A Caveat. *Journal of Magnetic Resonance Imaging* **2001**, *14* (1), 94–96. https://doi.org/10.1002/jmri.1157.
(43) Gossuin, Y.; Orlando, T.; Basini, M.; Henrard, D.; Lascialfari, A.; Mattea, C.; Stapf, S.; Vuong, Q. L. NMR Relaxation Induced by Iron Oxide Particles: Testing Theoretical Models. *Nanotechnology* **2016**, *27* (15), 155706. https://doi.org/10.1088/0957-4484/27/15/155706.
(44) Brero, F.; Basini, M.; Avolio, M.; Orsini, F.; Arosio, P.; Sangregorio, C.; Innocenti, C.; Guerrini, A.; Boucard, J.; Ishow, E.; et al. Coating Effect on the 1H—NMR Relaxation Properties of Iron Oxide Magnetic Nanoparticles. *Nanomaterials* **2020**, *10* (9), 1660. https://doi.org/10.3390/nano10091660.
(45) MacMahon, E.; Brougham, D. F. pH Dependence of MRI Contrast in Magnetic Nanoparticle Suspensions Demonstrates Inner-Sphere Relaxivity Contributions and Reveals the Mechanism of Dissolution. *Langmuir* **2023**, *39* (6), 2171–2181. https://doi.org/10.1021/acs.langmuir.2c02621.
(46) Kruk, D.; Korpała, A.; Taheri, S. M.; Kozłowski, A.; Förster, S.; Rössler, E. A. 1H Relaxation Enhancement Induced by Nanoparticles in Solutions: Influence of Magnetic Properties and Diffusion. *The Journal of Chemical Physics* **2014**, *140* (17), 174504. https://doi.org/10.1063/1.4871461.
(47) Félix-González, N.; Urbano-Bojorge, A. L.; Mina-Rosales, A.; del Pozo-Guerrero, F.; Serrano-Olmedo, J. J. Assessment of a Heuristic Model for Characterization of Magnetic Nanoparticles as Contrast Agent in MRI. *Concepts Magn. Reson.* **2015**, *44A* (5), 279–286. https://doi.org/10.1002/cmr.a.21361.
(48) Rollet, A.-L.; Neveu, S.; Porion, P.; Dupuis, V.; Cherrak, N.; Levitz, P. New Approach for Understanding Experimental NMR Relaxivity Properties of Magnetic Nanoparticles: Focus on Cobalt Ferrite. *Phys. Chem. Chem. Phys.* **2016**, *18* (48), 32981–32991. https://doi.org/10.1039/C6CP06012A.
(49) Girardet, T.; Diliberto, S.; Carteret, C.; Cleymand, F.; Fleutot, S. Determination of the Percentage of Magnetite in Iron Oxide Nanoparticles: A Comparison between Mössbauer Spectroscopy and Raman Spectroscopy. *Solid State Sciences* **2023**, *143*, 107258. https://doi.org/10.1016/j.solidstatesciences.2023.107258.
(50) *MathWorks - Makers of MATLAB and Simulink - MATLAB & Simulink*. https://www.mathworks.com/ **(accessed 2024-03-29)**.
(51) H, V. Das Temperaturabhangigkeitsgesetz Der Viskositat von Flussigkeiten. *Phys. Z.* **1921**, *22*, 645–646.
(52) Fulcher, G. S. Analysis of Recent Measurements of the Viscosity of Glasses. *Journal of the American Ceramic Society* **1925**, *8* (6), 339–355. https://doi.org/10.1111/j.1151-2916.1925.tb16731.x.
(53) Tammann, G.; Hesse, W. Die Abhängigkeit Der Viscosität von Der Temperatur Bie Unterkühlten Flüssigkeiten. *Zeitschrift für anorganische und allgemeine Chemie* **1926**, *156* (1), 245–257. https://doi.org/10.1002/zaac.19261560121.

TOC

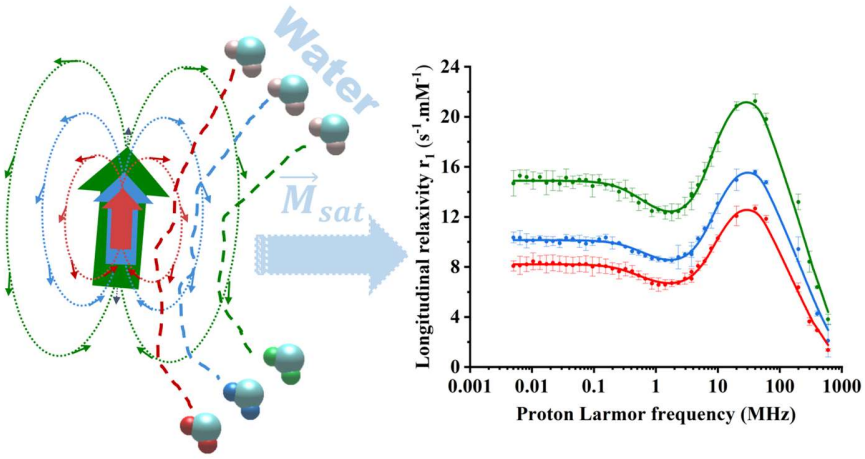
Water
$\vec{M}_{sat}$
Longitudinal relaxivity r_1 ($s^{-1}.mM^{-1}$)
24
20
16
12
8
4
0
0.001
0.01
0.1
1
10
100
1000
Proton Larmor frequency (MHz)